Geophysical Journal International

Geophys. J. Int. (2023) **235,** 2094–2106
Advance Access publication 2023 September 11
GJI Applied and Marine Geophysics

https://doi.org/10.1093/gji/ggad346

Ultrahigh-resolution 9C seismic survey in a landslide prone area in southwest of Sweden

Tatiana Pertuz and Alireza Malehmir

Department of Earth Sciences, Uppsala University, Villavägen 16, SE 75236, Uppsala, Sweden. E-mail: tatiana.pertuz@geo.uu.se

Accepted 2023 August 27. Received 2023 August 8; in original form 2023 February 14

SUMMARY

We studied the benefits of a nine-component (9C) seismic survey over a landslide-prone area in southwest of Sweden to retrieve ultrahigh-resolution shear wave reflection images of the subsurface as well as crucial information on physical properties of the sediments. A complete, 1 m shot and receiver spacing, multicomponent 2-D seismic profile was acquired using three-component microelectromechanical-system-based landstreamer receivers, and a 5-kg sledgehammer strike in vertical and horizontal orientations as three-component seismic source. Given the rich number of shear wave reflections observed on all the 9C data, the processing work focused on their retrievals. It revealed three distinct reflections, two of which associated with coarse-grained materials and one with an extremely undulating bedrock surface. Given the extremely slow shear wave velocities on the order of 60–100 m s^{-1}, we obtained ultrahigh-resolution shear wave sections avoiding temporal and spatial aliasing. Imaging results suggest vertical-source and horizontal-radial receiver ($V–H_R$), and horizontal-transverse source–receiver orientations ($H_T–H_T$) provided the most optimum images of the subsurface. A non-hyperbolic algorithm was applied to the normal-moveout corrections justified by the traveltime differences of the bedrock reflection in different shear wave sections. The improved images by incorporating the anisotropy term suggest that the data set reveals moderate shear wave anisotropy along some portions of the profile. The *Vp*/*Vs* ratio obtained by using bedrock reflection in *P*- and *S*-wave sections suggests values ranging 10–16, which implies high water content. Areas with lower *Vp*/*Vs* coincides with greater anisotropic parameters and this can indicate disturbed clays or presence of sensitive clays.

Key words: Image processing; Seismic anisotropy; Wave propagation.

1 INTRODUCTION

Potential of multicomponent seismic surveys has not yet fully been explored for near-surface investigations as compared with mineral and hydrocarbon exploration (Miles 1988; Pugin *et al.* 2009). In the last decade, development in multicomponent seismic methods has broaden experience and knowledge for near-surface applications despite that this is considered an expensive technology (Kristiansen & Waggoner 2005; Pugin *et al.* 2009; Brodic *et al.* 2015; Farfour & Yoon 2016). For near-surface studies, seismic methods have strengthened their role over other geophysical methods commonly used for landslide studies, which are typically ground-penetrating radar (GPR), electrical resistivity tomography (ERT), controlled source and radio magnetotellurics (RMT). However, as it is demonstrated, for instance, by Dasios *et al.* (1999) and Malehmir *et al.* (2013a), seismic methods can complement these commonly used geophysical methods in clay-rich settings, and where sediments are highly saturated, and where most geoelectric- and electromagnetic-based methods would suffer low resolution and penetration depth because of the conductive nature of the clayey medium. Moreover, some advantages have been shown for shear wave (*S*-wave) reflection surveys in areas where compressional-wave (*P*-wave) reflection surveys have shown limitations in resolving small scale, still important, structures (Pugin *et al.* 2004, 2009; Bansal & Gaiser 2013; Malehmir *et al.* 2013a). Multicomponent studies in near-surface applications have great potentials and should be done to complement the conventional *P*-wave surveys.

The ultimate application of a multicomponent seismic survey is to employ a nine-component (9C) acquisition setup using three-component (3C) receivers and, also, 3C sources. The data then will be rich in information, also possible anisotropic information (Stewart 1994; Ata & Michelena 1995; Pugin *et al.* 2009; Gupta *et al.* 2015). To the best of our knowledge, such data sets are used for purposes such as reservoir characterization, detecting fluid content in sediments and improved understanding of wave propagation in complex anisotropic media. Given that seismic waves propagate differently in different materials, their capture and analysis can reveal more information about the subsurface (Li & Zhang 2011;

© The Author(s) 2023. Published by Oxford University Press on behalf of The Royal Astronomical Society. This is an Open Access article distributed under the terms of the Creative Commons Attribution License (https://creativecommons.org/licenses/by/4.0/), which permits unrestricted reuse, distribution, and reproduction in any medium, provided the original work is properly cited.

Downloaded from https://academic.oup.com/gji/article/235/3/2094/7269211 by Uppsala Universitetsbibliotek user on 22 November 2023

Farfour & Yoon 2016) and for predicting fluid distribution (Qian *et al.* 2007). Nine-component data if properly acquired are the most complete solution for this purpose. This type of data set allows the observation of not only primary waves but also converted waves such as radial (*SV*) and transverse (*SH*) shear waves for different propagation directions (Stewart *et al.* 2003; Hu *et al.* 2004; Pugin *et al.* 2009; Pugin & Yilmaz 2019). They can inherently also allow improved resolution given the slower velocity of the shear waves and their typically smaller wavelength compared to the *P* waves.

Multicomponent seismic surveys over normally consolidated clay deposits can particularly be of great relevance. These deposits can sometimes have extremely slow shear wave velocities on the order of 100–300 m s^{-1}, which means a great or ultrahigh resolution for shear wave imaging. Sedimentologically, grain shape of clay particles are elongated and usually deposited in layers at the presence of strong covalent bonds in between them (Weaver & Pollard 1973; Brigatti *et al.* 2006; Sayers & Den Boer 2016). Clay structures can hold large quantities of water due to their high porosity, however, an excessive stress on their skeleton can lead to collapsed structures known as 'quickness', sometimes referred as 'sensitive clays'. Nevertheless, other properties such as pore water pressure, shear stress, load, among others, are dependent on the amount of water in the clay skeleton (Torrence 2012; Sayers & Den Boer 2016; Solberg *et al.* 2016). These types of clays, quick or sensitive clays, are mostly present in the northern countries (e.g. Sweden, Canada and Norway) resulted from leaching their salt content by fresh water infiltration due to the isostatic uplift after the last deglaciation around 10–11 kyr ago (Torrance 2012). These clays when undisturbed and unleached show 'card house' structures, and when leached but undisturbed, the house structures collapse. However, holding high-water content and when they are remoulded, leads to totally collapsed clay structures resulting in their liquefaction phenomena (Gylland *et al.* 2013). This means, in seismic terms, quick clays have more of laminar texture than undisturbed clays and if this is registered, one should be able to point at areas where these deposits are present. Given the extreme slow shear wave velocity (on the order of 60–100 m s^{-1}) of quick-clay settings (Malehmir 2019, 2021), it is worthwhile performing test seismic surveys to evaluate if these laminated structures can somewhat be recorded in multicomponent data.

In two series of field campaigns in 2011 and 2013, several geophysical and geotechnical methods were carried out to better understand the possible formation and presence of quick-clay deposits. The test site is located in southwest of Sweden near to the historical Göta River landslide that occurred in 1957 (Odenstad 1958), which costed environmental damages as well as human lives. As part of the geophysical campaigns, several seismic lines were acquired, boreholes were drilled and samples analysed, electromagnetics, magnetic and gravity profiles were measured as well (Malehmir *et al.* 2013a). Outcomes of these surveys highlighted the use of seismic methods in clayey media due to their improved depth penetration (40–80 m) and the ability to differentiate contrasting layers within the sediments (Lundström *et al.* 2009; Malehmir *et al.* 2013a, b, 2016b; Polom *et al.* 2013; Adamczyk *et al.* 2014; Lundberg *et al.* 2014; Shan *et al.* 2014; Salas-Romero *et al.* 2016, 2019, 2021; Wang *et al.* 2016; Malehmir 2019). While revisiting the data, Malehmir (2019, 2021) explored that remarkable shear wave energy with a velocity on the order of 60–120 m s^{-1} was also recorded on the vertical component data. This justified a new acquisition work in 2020 (along Line 1 in Fig. 1) using both vertical component data as well as 3C recorders but having much smaller spacing to allow recording of unaliased shear waves (Pertuz & Malehmir 2021, 2023). As a follow-up, the current study focuses on the 3C recorded data set of 2020 survey (Fig. 1), but also shots generated in three directions forming a complete 9C data set. This is the first time such a data set is reported from the site and overall, for quick-clay studies. Nearby the study area, there are clear signs of retrogressive quick-clay landslides, hence, their presence (i.e. seen as landslide scars nowadays) are most likely along the renewed seismic line (Fig. 1a). The study area is characterized by large clay deposits (up to 80 m thick) overlying an extremely undulating crystalline bedrock (Malehmir *et al.* 2013a).

In this work, we explore the potential of the 9C seismic data set acquired in 2020. The results presented and discussed are based on derived *P-P* and *S-S* wavefield reflection seismic sections, which image the entire setting with ultrahigh-resolution (0.5–1 m) down to bedrock. In order to explore the anisotropy effect on the data, velocity analysis took advantage of an additional term incorporating a non-hyperbolic moveout correction. The main objectives of the study are therefore: (1) present the data quality of the 9C data and subsequent imaging of their *S-S* wavefields, and (2) provide insight on the nature of the results and benefit of 9C data acquisition works for quick-clay landslide studies.

2 SEISMIC DATA ACQUISITON

The seismic data were acquired along a 2-D line with a collocated and partly simultaneously recorded single-component data set recently presented by Pertuz & Malehmir (2023). The goal of the single-component vertical-type survey was also to illustrate that significant amount of shear wave is available in these setups and can be used, if properly acquired, in order to retrieve ultrahigh-resolution reflection sections. The 9C data set was recorded alongside the vertical shots of the single-component data; however, additional shots were generated using horizontal strikes. The line extends approximately 240 m long and was acquired using a roll-along geometry employing a landstreamer of 120–3C units (Fig. 2a), which was totally moved to the second part of the line to complete the total profile length with no overlapping parts. A 3C-microelectromechanical-system-based (MEMS) seismic landstreamer was used for this purpose (Brodic *et al.* 2015; Malehmir *et al.* 2016b) with 1 m receiver spacing, with a broad natural frequency range of 0–800 Hz. At each shot position, collocated with the receivers, that is, at every 1 m, three repeated shot records were generated with a 5-kg sledgehammer in vertical (V) direction on a flat steel-base plate (Fig. 2b) and then in an inline-horizontal (H_R), and crossline-horizontal (H_T) directions on an H-shaped steel-base plate (Fig. 2c). The recording used 1 ms sampling rate and 3000 ms record length to ensure that slow-velocity wave modes are contained in the data down to bedrock at approximately 40–50 m depth (Malehmir *et al.* 2016b; Salas-Romero *et al.* 2016; Pertuz & Malehmir 2023). Table 1 summarizes the seismic data acquisition parameters of this study. The geodetic surveying was done using an accurate differential GPS system providing an accuracy on the order of a few centimetres. The seismic line was acquired in two days. While weather condition was good on the first day, the second day was strongly windy and partly influenced the data quality.

3 SEISMIC DATA PROCESSING AND WORKFLOW

Data processing for the acquired 9C data set followed a conventional processing workflow (Table 2) assuming that the reflections are of pure nature, that is, *P-P* and/or *S-S*. Therefore, the processing was

Downloaded from https://academic.oup.com/gji/article/235/3/2094/7269211 by Uppsala Universitetsbibliotek user on 22 November 2023

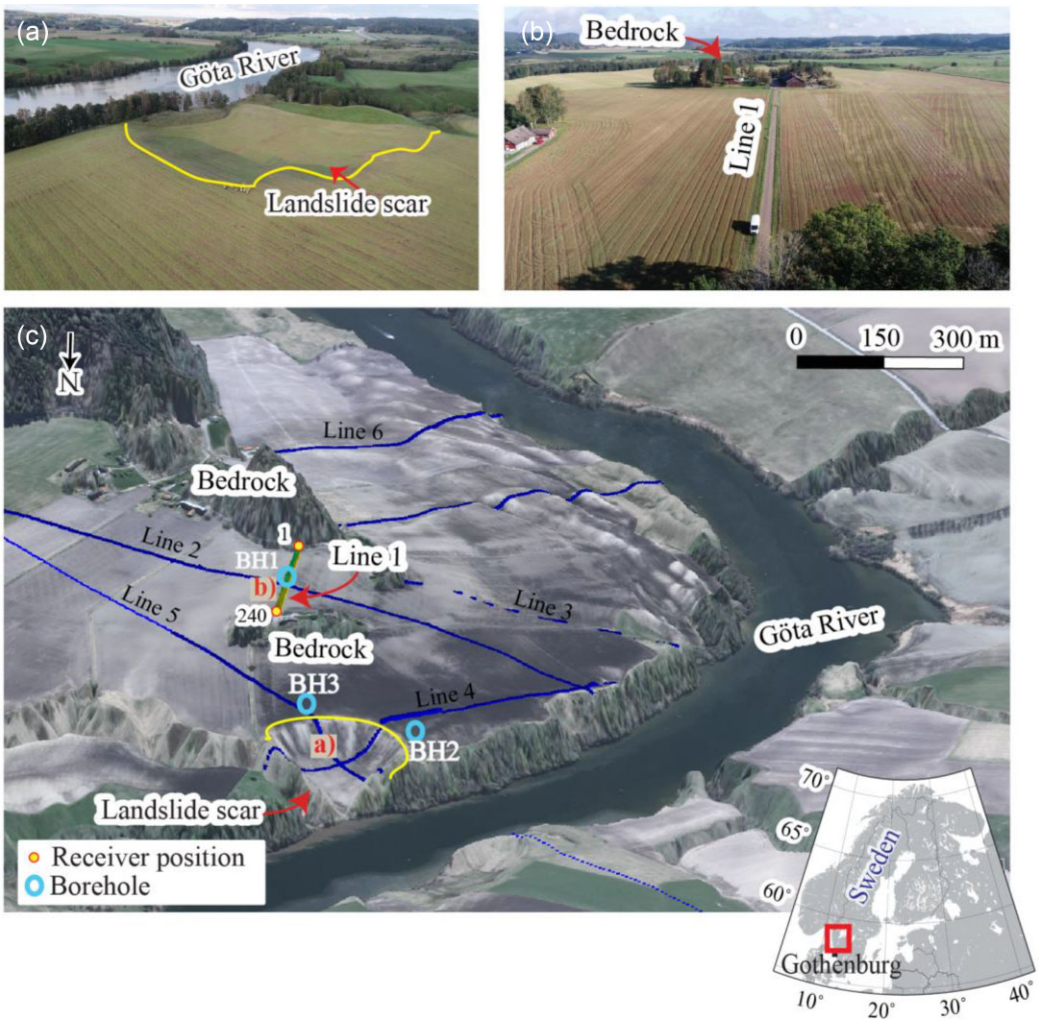

Figure 1. Study area near the city of Lilla Edet in southwest of Sweden. (a) UAV picture of a landslide scar close to the acquisition line, (b) aerial photo of the seismic line of this study where both ends, where trees are present, show bedrock outcrops, and (c) aerial photo draped on the Lidar topography surface showing various seismic lines acquired during 2011–2020 in the study area. A new seismic data set was acquired in 2020 along Line 1 (green line) involving a high-fold vertical component (Pertuz & Malehmir 2023) and a 9C recording work. In yellow, the landslide scar shown in (a) is marked.

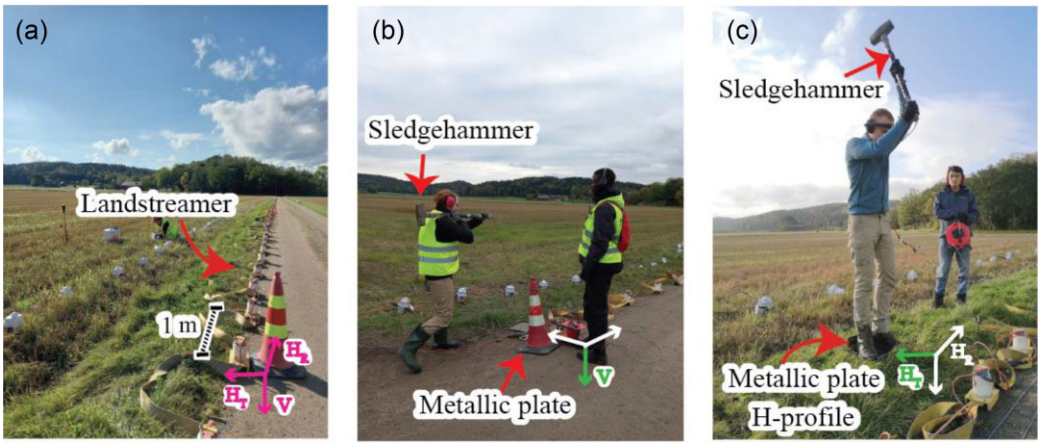

Figure 2. A collection of field photos from the seismic acquisition. (a) MEMS-based landstreamer was used for the data recording; on the source side, a 5-kg sledgehammer was used to impact in (b) vertical direction (V) over a flat-metallic base plate and (c) horizontal directions (radial, H_R, and transverse, H_T) on an H-shaped metallic base plate. Arrows indicate receiver- (magenta) or source orientations (green).

Downloaded from https://academic.oup.com/gji/article/235/3/2094/7269211 by Uppsala Universitetsbibliotek user on 22 November 2023

Table 1. Seismic data acquisition parameters of 2-D 9C survey (2020) using the MEMS-based 3C landstreamer in the study area (Lilla Edet, Sweden).

Source parameters	Source type	Weight drop: 5-kg sledgehammer
	Source orientation	Vertical and horizontals (radial and transverse)
	Shot spacing (m)	1
	Shots per point	3
Recording parameters	Receiver type	MEMS-based landstreamer
	Receiver orientation	Vertical, radial and transverse
	Number of receivers	120
	Receiver interval (m)	1
	Frequency range (Hz)	Broad-band (0–800 Hz)
	Record length (ms)	3000
	Sampling rate (ms)	1
Survey parameters	Receiver-line direction	SW-NE
	Geometry and acquisition type	2-D land
	Survey design	Roll-along pattern
	Data set components	9
	Maximum offset (m)	120
	Meteorological season	Autumn Day1: Sunny; Day2: Windy

Table 2. Key processing steps and parameters for *P-P* and *S-S* wavefields reflection imaging of the 2020 9C seismic data set.

Step	Process	Processing workflow Conventional
1	Data input	SEGD format
2	Trace edit	Kill noisy traces
3	Geometry	CMP binning: 0.5 m
4	First break picking	Automatic and manual
5	Median Filter	330 m s^{-1} to remove airwave
6	Wiener deconvolution	Gap: 26 and 33 ms and length: 150 ms
7	Bandpass filter	*P* wavefield: 15–30–200–210 Hz and *S* wavefield: 20–40–90–110 Hz
8	Spectral equalization	*P* wavefield: 30–35–190–200 Hz and *S* wavefield: 20–35–70–100 Hz
9	Residual statics	Surface consistent
10	AGC	250 ms
11	NMO corrections	60 per cent stretch
12	Stack	Unity
13	FX-deconvolution	Filter length: 16 ms Window length: 100 ms Window width: 12 traces
14	Migration	Phase shift (constant velocity *S* wave = 100 m s^{-1} and *P* wave = 1400 m s^{-1})

only focused on these wavefields in the 9C data. Malehmir (2019 and 2021) as well as Pertuz & Malehmir (2023) showed the *S-S* reflections are strong, and their imaging can be done using simple Common midpoint (CMP) processing workflows even in the vertical component data. In the first step, vertical stacking for the repeated shot records was done for each component to improve signal-to-noise ratio. Fig. 3 shows an example of a raw shot gather grouped by source orientation and recorded in three different receiver orientations, which evidence the recorded high-quality data. For the shot gathers in each source–receiver-orientation strong hyperbolic reflections are captured at about 0.3, 0.35 and 0.55 s, labelled as S1, S2 and B consistent with the previous observations reported in the area on the vertical component data (Malehmir *et al.* 2016b; Salas-Romero *et al.* 2016; Pertuz & Malehmir 2023). As a quality control, noisy and dead traces were removed from each shot gather. In multicomponent seismic data acquisition, the recorded wavefield is captured in an inline-crossline system (Hardage *et al.* 2011). For this reason, a source–receiver rotation was performed to populate horizontal component data to *SV* and *SH* or radial and transverse components. The seismic line is rather on a flat surface with a maximum of 30 cm elevation difference. Given our interest in the sediments above bedrock, a shallow ground water table (of only 1 m, Salas-Romero *et al.* 2016), and the high-quality reflections in the raw shot gathers, we decided to ignore the application of refraction static corrections for both *P-P* and *S-S* wavefields. Instead we relied on the surface-consistent static correction solution to handle any static issues in the data.

At the pre-stack processing stage, coherent noise (i.e. produced by surface waves and airwaves) was attenuated using, for example, a median filter, which used a velocity of 92 and 330 m s^{-1}, respectively. Some of the shots presented a ringing effect that was classified as multiples. Therefore, a wiener deconvolution filter allowed removing some repeated energy without altering the amplitude spectrum of the shot. In order to improve the quality of reflections, a bandpass filter was applied to reduce mainly the low frequency, from surface waves remained, in the data (Fig. 4b). Given the nature of the recorded seismic events, corner frequencies were set separately for *P-P*, 15–30 and 200–210 Hz, and *S-S*, 20–40 and 90–110 Hz, wavefield imaging following the previous work of Pertuz & Malehmir (2023). The fact that the wavelength of the *P*-wavefield data is on the order of 10–15 m (for a *P*-wave velocity of 1400 m s^{-1} and a dominant frequency of 100–150 Hz), in such a near-surface conditions, they do not add a great reflection imaging value for a target depth down to 40–50 m. However, refracted wavefield maps reasonably well the undulating bedrock well and this is illustrated in the earlier studies including the most recent one by Pertuz & Malehmir (2023). *S-S* reflections are clearer, not contaminated by the source-generated noises, and arrive at later time with much greater resolution (approximately 1–2 m for an *S*-wave velocity of 100 m s^{-1} and a dominant frequency of 50–100 Hz) helping to partly improve the temporal resolution of the data and attenuate strong surface waves (Fig. 4c). An *FK* filter was used to eliminate

Downloaded from https://academic.oup.com/gji/article/235/3/2094/7269211 by Uppsala Universitetsbibliotek user on 22 November 2023

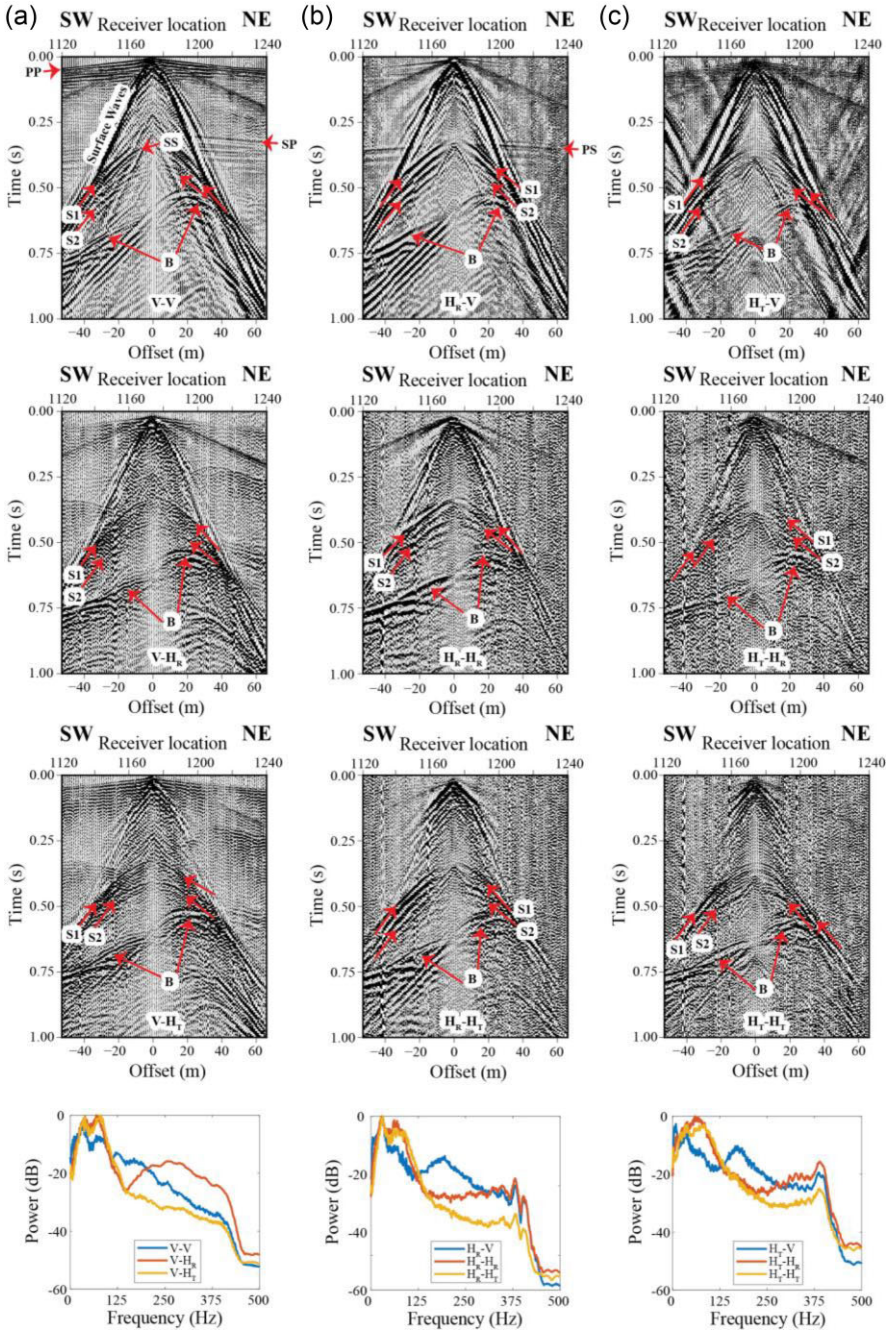

Figure 3. An example raw shot gather generated in three different orientations on the 3C receivers of the landstreamer. (a) Vertical-source orientation recorded in vertical, radial and transverse components, (b) radial-source orientation recorded in vertical, radial and transverse components, and (c) transverse-source orientation recorded in vertical, radial and transverse components. The amplitude spectra plots showing the frequency content of the shots in different orientation. Reflections marked as S1, S2 and B are judged to be of pure shear nature although show different quality in different source–receiver orientations. They clearly occur within the cone of the shear wave arrivals. Other events are also recognizable beyond this cone that are likely other wave modes, such as *P-S*, *S-P* and dispersive surface waves (Raleigh and love waves). Raleigh waves are mainly produced by vertical sources and because the vertical particle motion, are detected in vertical and radial components. Love waves are generated by pure *SH* sources and travel with horizontal particle motion, hence seen dominantly in the transverse component.

any remaining coherent and linear noise generated by the strong wind during the second day of data acquisition.

Velocity analysis was conducted by looping surface-consistent residual statics, normal-moveout (NMO) corrections and horizontal stacking the processed shot gathers. NMO corrections were applied to image separately *P-P* from *S-S* reflection wavefields. Velocity models ranged 1200–1500 and 60–120 m s^{-1} for each wavefield, respectively. Consequently, sections were normalized to unity and conventionally stacked as a function of their common-depth point (CDP).

In the post-stack steps, *P-P* and *S-S* were subject to FX-deconvolution filter to help improve continuity of the reflections. A phase-shift post-stack time migration method was then applied using a constant velocity of 1400 and 100 m s^{-1}, respectively, to

Downloaded from https://academic.oup.com/gji/article/235/3/2094/7269211 by Uppsala Universitetsbibliotek user on 22 November 2023

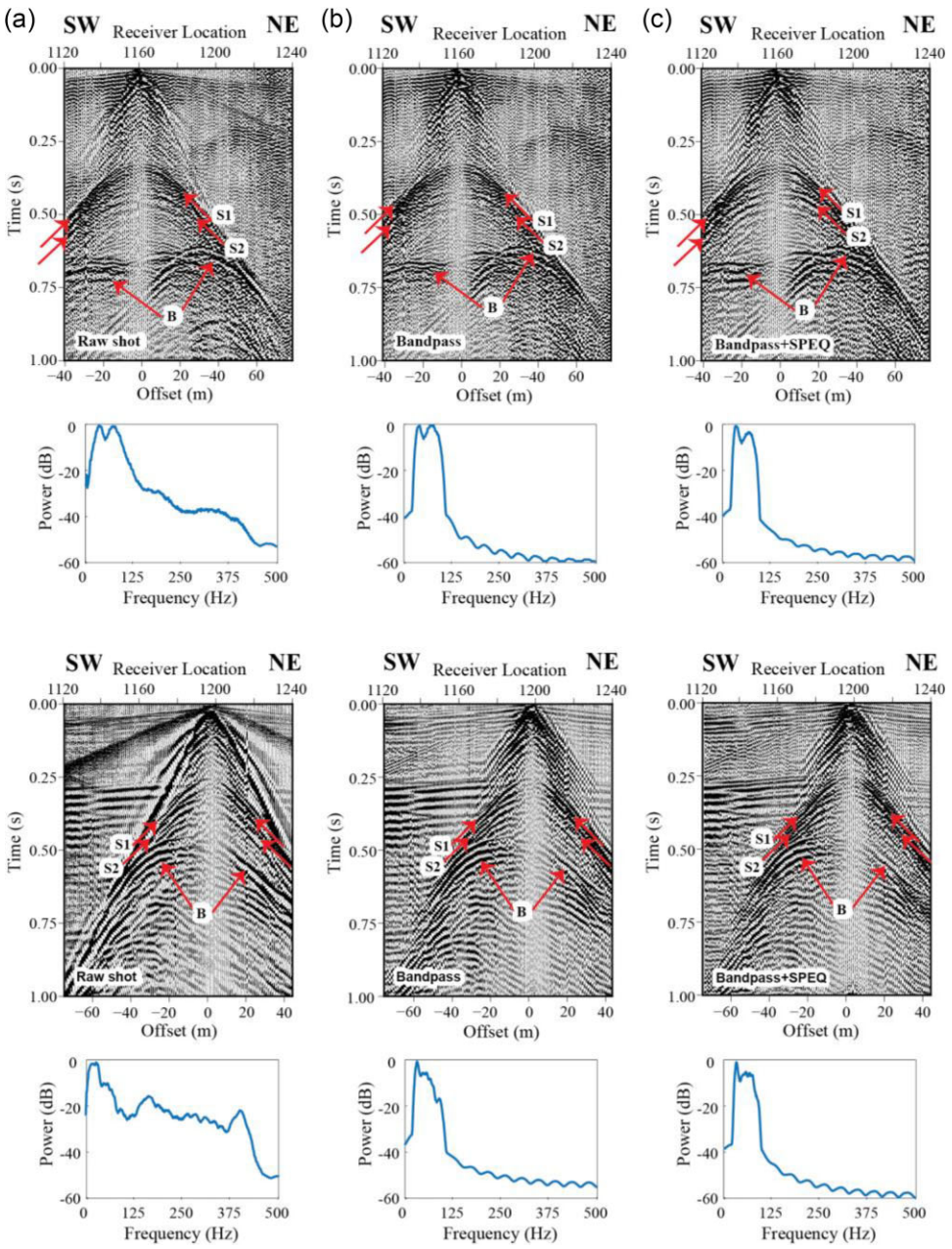

Figure 4. Effect of different processing steps on two example shot gathers, source–receiver orientation H_R–V and V–H_T, respectively. The amplitude spectrum is displayed for each shot gather in every processing step. (a) Raw shot gathers showing a frequency bandwidth of 4.5–400 Hz, although much the energy is contained up to 120 Hz. (b) Bandpass filter applied with frequency corners of 20–40 and 90–110 Hz. (c) Spectral equalization filter using a corner frequency of 20–35 and 70–100 Hz.

migrate both *P-P* and *S-S* sections. *P-P* section was only derived from vertical-source and receiver orientations because it is the optimal source–receiver orientation for *P-P* reflection energy (Hardage *et al.* 2011; Pugin & Yilmaz 2019). Nonetheless, much of the focus was given to the *S-S* section derived from all the 9C data as they were captured in all components.

3.1 Non-hyperbolic normal moveout

Given the higher sensitivity of the shear wave energy to an anisotropic medium, a non-hyperbolic NMO4 correction was applied in the seismic processing workflow (Alkhalifah & Tsvankin 1995; Alkhalifah 1997; Tsvankin, 2005). The velocity model, for NMO4 corrections, used the output of the conventional velocity analysis, however, included an additional term (ζ) in the NMO equation (eq. 1), first described by Alkhalifah & Tsvankin (1995) then adapted for *S* wave by Li & Yuan (2003),

$$t_S^2 = t_{S0}^2 + \frac{x^2}{V_{S2}^2} - \frac{2\zeta x^4}{V_{S2}^2\left[t_{S0}^2 V_{S2}^2 + x^2\right]} \tag{1}$$

where t is the *S*-wave two-way traveltime, V_{S2} is the *S*-wave velocity from NMO, ζ is an anisotropic term and x is the offset. NMO4 correction was applied to all *S-S* wavefield seismic sections, motivated by the not-flattening effect in reflections, after the NMO corrections, especially at far offsets.

Downloaded from https://academic.oup.com/gji/article/235/3/2094/7269211 by Uppsala Universitetsbibliotek user on 22 November 2023

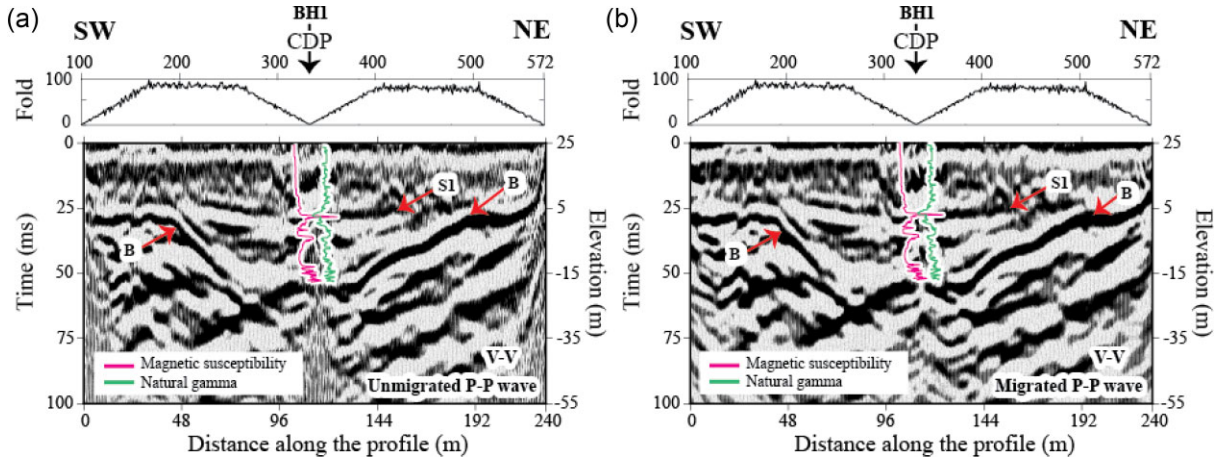

Figure 5. (a) Unmigrated and (b) migrated, using a constant velocity of 1400 m s^{-1}, *P-P* wavefield reflection stacked section of Line 1 obtained using vertical-source–receiver orientation. Given the fixed geometry (shoot-through) and one-time roll-along nature of the data, the CDP fold coverage (plotted on top of the sections) drops to zero in the middle of the line. Although rather poorer quality than the *S-S* wavefield data, the undulating bedrock interface is recognizable and labelled as B, as well as a set of coarse-grained layer labelled as S1, which are both confirmed by logging data from borehole BH1 that measured magnetic susceptibility and natural gamma intersecting these layers.

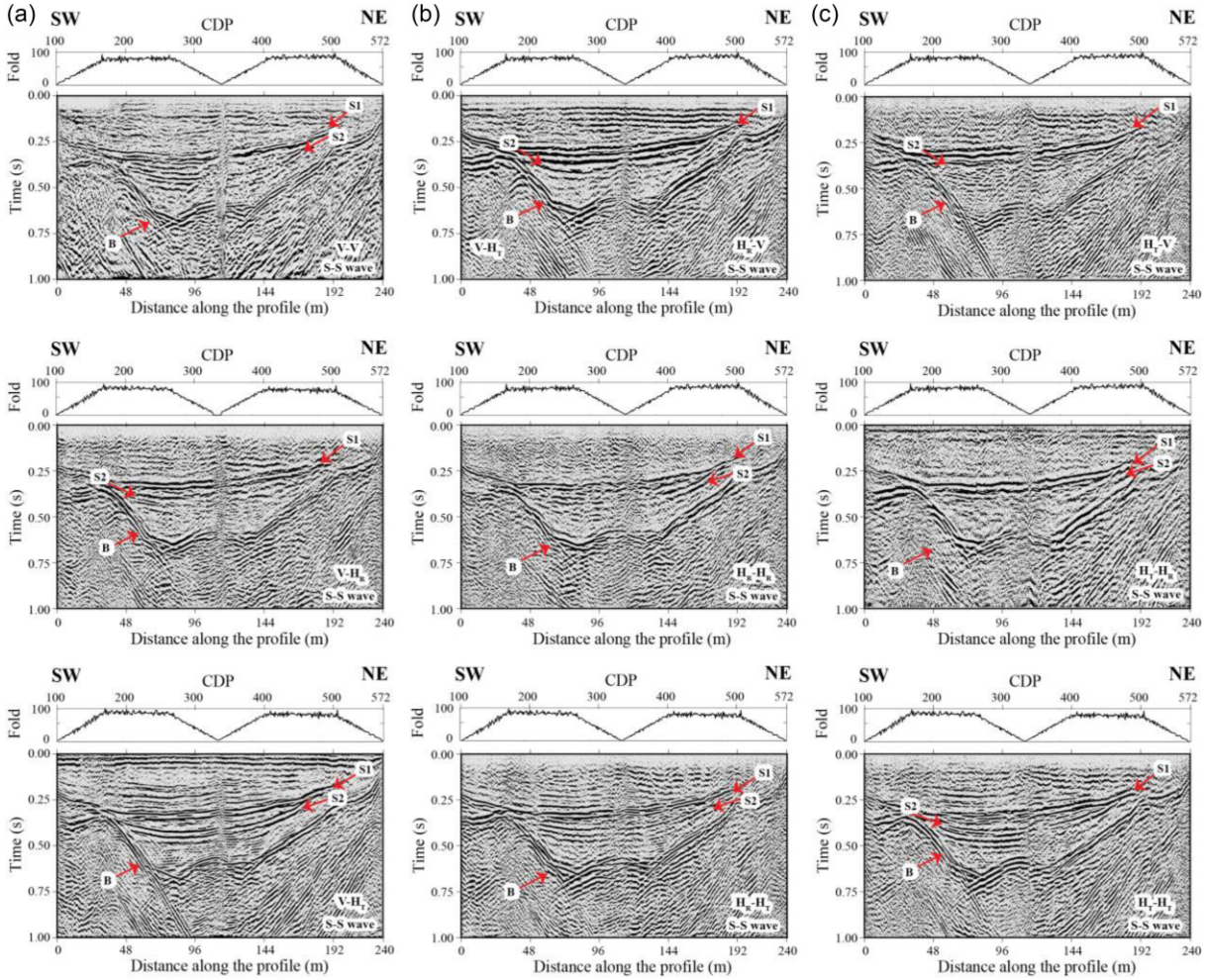

Figure 6. *S-S* wavefield sections derived from all the 9C data along Line 1. (a) Vertical, (b) radial and (c) transverse source orientations recorded on vertical (top), radial (middle) and transverse (bottom) receiver orientations. Each section suffers a zerofold coverage in the middle due to the seismic data acquisition setup. All sections image S1 (shallow coarse-grained materials), S2 (deeper coarse-grained materials) and B (bedrock) in high quality although their arrival times and appearance are slightly different depending on the source and receiver orientations used.

Downloaded from https://academic.oup.com/gji/article/235/3/2094/7269211 by Uppsala Universitetsbibliotek user on 22 November 2023

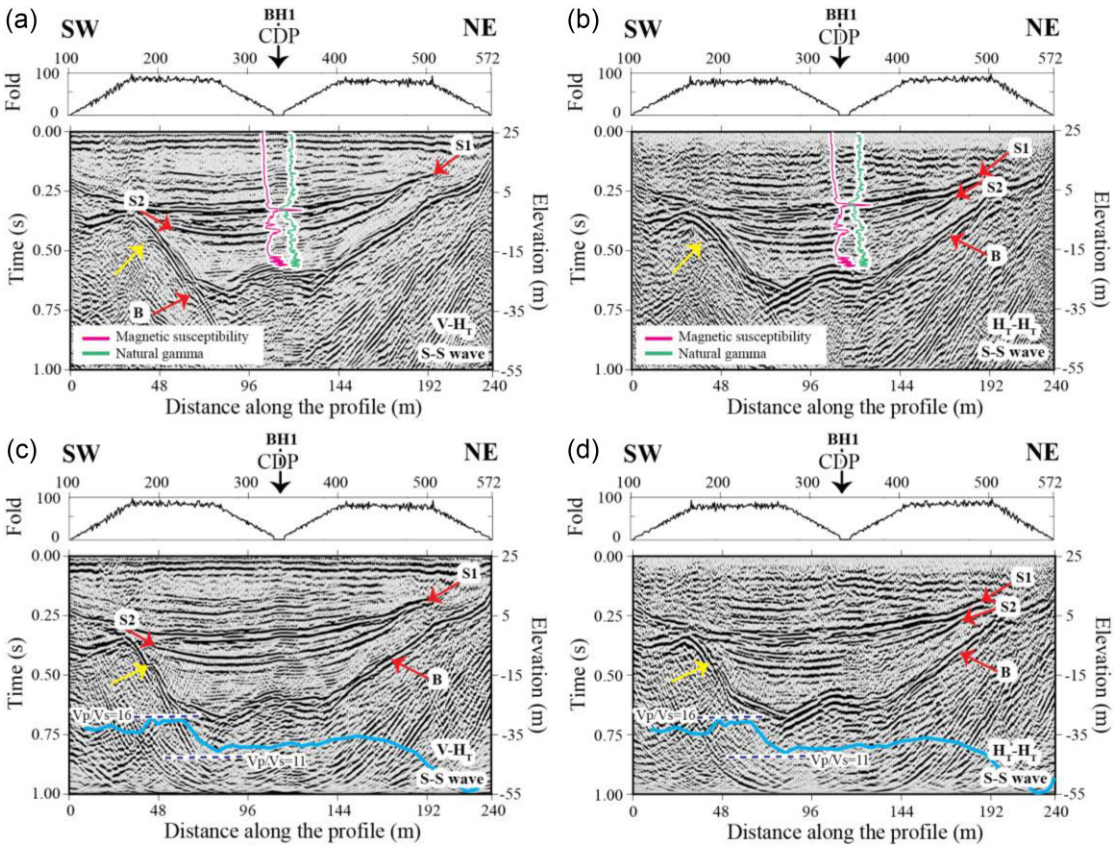

Figure 7. Judged to be the optimum source–receiver orientations for *S-S* reflection imaging from the acquired 9C data set. (a) and (b) Unmigrated and (c) and (d) migrated *S-S* stacked sections for V-H_T and H_T-H_T source–receiver orientations, time-to-depth converted using a constant velocity of 100 m s^{-1}. Several reflections can be identified in the sections including a shallow reflection, *S*1, appearing at about 0.25 s, generated from coarse-grained materials, a nearly subparallel, underlying reflection, *S*2, at about 0.3 s, generated also from coarse-grained materials, and a deeper undulating reflection, B, at varying arrival times but deepest at 0.6 s, originated from a crystalline bedrock. A strong *S-S* diffraction marked using the yellow arrow, in the unmigrated sections, is likely generated from a small step in the bedrock showing the great resolution provided by the 9C data set. *Vp*/*Vs* profile is overlapped in V-H_T and H_T-H_T sections indicating a maximum of 16 and minimum of 11, which is a good indication of high-water content in the sediments.

4 RESULTS

High-quality shot gathers as shown in Figs 3 and 4(a) are an indicator of a good ground-sensor coupling even for the landstreamer sensor. Earlier at the pre-stack processing stage, two shallow reflections (S1 and S2) and a complex one (B) were recognizable with different amplitude strength depending on the source–receiver orientations. As anticipated, first breaks are mostly recognizable in the vertical-source–receiver orientation, also recorded but weak in other orientations. Visible differences on each receiver orientation are noted when comparing their amplitude spectra, in Fig. 3, by source orientation. H_T receiver orientation shows lower signal power than other components for V and H_R source orientations.

P-P reflection section compared with borehole logging data, in Fig. 5, suggests an undulating bedrock and a sand-silty layer presence from 30 to 70 ms. The undelaying layer of sandy-silt layer is not well resolved because of lower *P-P* seismic resolution. The sand-silty layers are separated by less than 7 m thickness of clay and this clearly can be used as a proxy for the vertical resolution. Fig. 6 shows the results of the reflection data processing of *S-S* wavefield for all the 9C data. The sections are shown in a matrix organization in which source orientations (first label) and receiver orientation (second label) are grouped and labelled as V (vertical), H_R (horizontal radial) and H_T (horizontal transverse), respectively. Processing steps applied on the data were effective and helped imaged reflections B, S1 and S2 in great details. Smaller and shallower reflections are also visible, however, do not show a continuous nature as these three sets of reflections.

The S2 reflection is imaged in most of the *S-S* sections, but less favoured in the H_T-V source–receiver orientation. On contrary, the *S*2 reflection is imaged better by the H_T receiver and vertical-impact source orientations (Fig. 6a, bottom). The S2 reflection in the V-H_T shows a well-defined character not seen in any of the other *S-S* sections nor in any of the previous seismic data sets from the study area along the same line. The best *S-S* image is obtained using H_T source–receiver orientation (Fig. 6c, bottom). This may be expected since even the raw shot gathers (Fig. 3c) show clearer expression of the reflections, especially for the shallower one (S1) in this source–receiver orientation. The bedrock reflection (B) is imaged with strong amplitude in all the source–receiver orientations.

5 DISCUSSION

Contrary to the earlier seismic surveys previously conducted at the site and along Line 1 (Malehmir *et al.* 2016b; Salas-Romero *et al.* 2016, 2019, 2021; Wang *et al.* 2016; Malehmir 2019), this is the first time a 2-D 9C seismic data set is acquired with high-fold and fine shot and receiver spacing satisfying better an unaliased shear

Downloaded from https://academic.oup.com/gji/article/235/3/2094/7269211 by Uppsala Universitetsbibliotek user on 22 November 2023

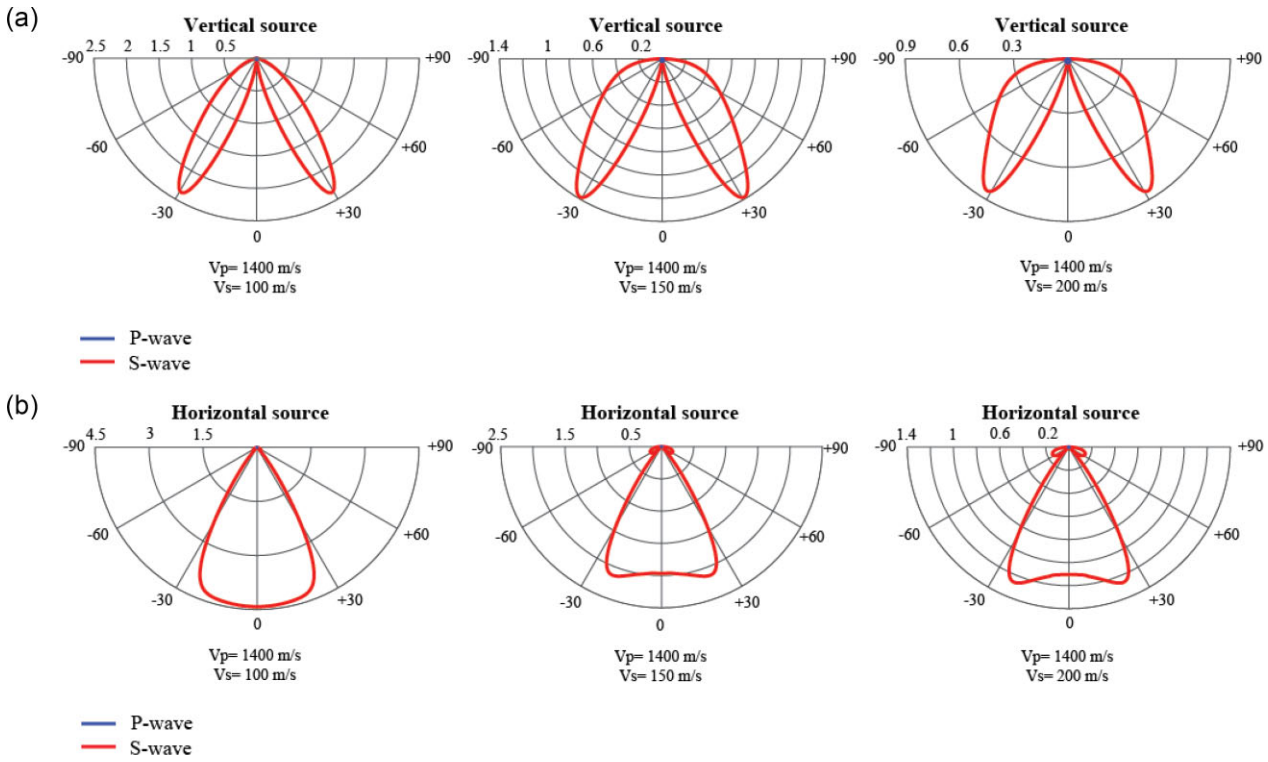

Figure 8. Radiation pattern for (a) a *P*-wave source with a medium velocity of 1400 m s^{-1} and (b) a variable *S*-wave source with a medium velocity of 100, 150 and 200 m s^{-1}. Given the physical property condition of the site, it is evident why *S*-wave energy is strong in the data. In vertical-source orientation, *S* wave (in a radial mode) propagates in a narrow take-off angle of around $\pm$ 30°, while for the horizontal source, the energy is broad but within the same range. *S*-wave radiated energy is significantly larger than the *P* wave. This also supports while most of the *S*-wave reflections occur in a narrow-offset window as shown in Fig. 3. Source code was provided by H. Jodeiri and is based on Miller & Pursey (1954), and presented in Yilmaz *et al.* (2022).

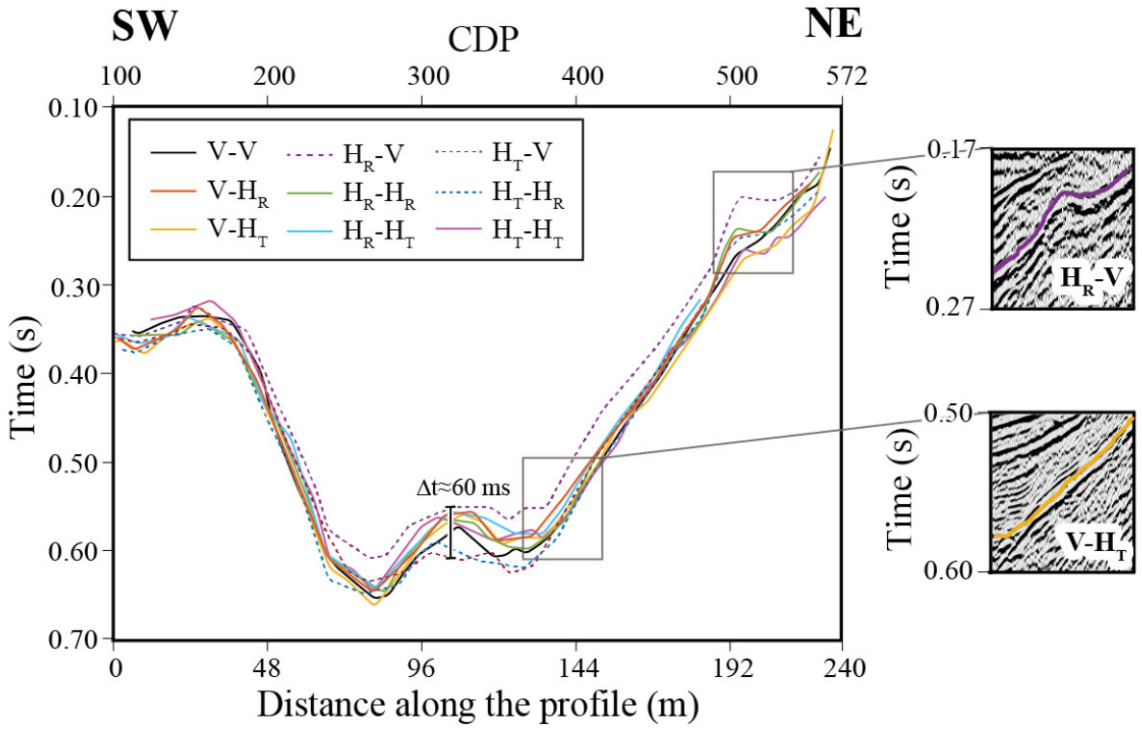

Figure 9. *S-S* traveltime delays from the bedrock seismic reflection (B) in the 9C sections. Bedrock reflection arrives at different times depending on the source–receiver orientation. Reflection B at H_R-V section is the fastest, while it is the slowest at H_T-V, H_T-H_R and V-V sections. The time difference, approximately 60 ms, shows signs of shear wave splitting because of the anisotropic nature of the medium.

Downloaded from https://academic.oup.com/gji/article/235/3/2094/7269211 by Uppsala Universitetsbibliotek user on 22 November 2023

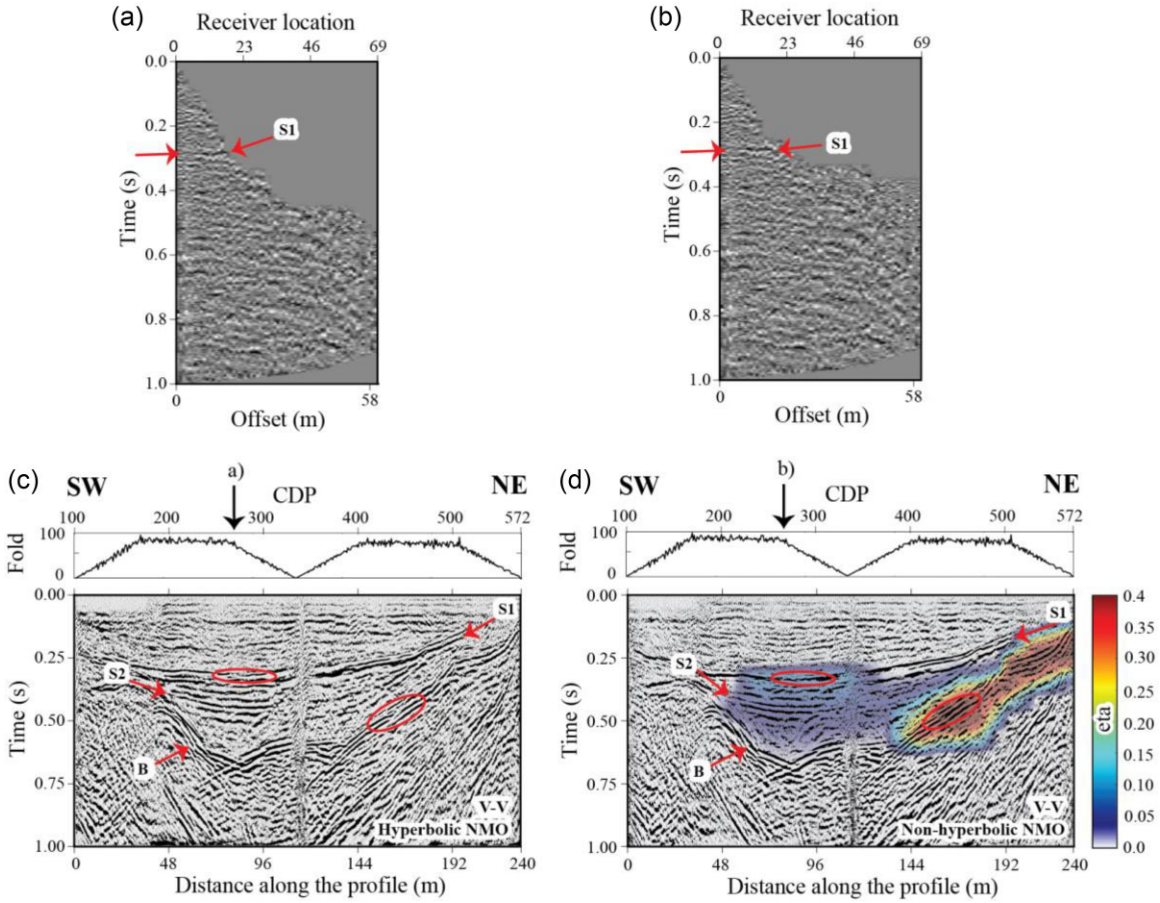

Figure 10. Example of a CDP gather with (a) only NMO corrections and (b) additional NMO4 corrections applying an additional term, which includes *eta* parameter. Vertical-source–receiver orientation unmigrated stacked section using (c) only an NMO hyperbolic correction and (d) NMO non-hyperbolic correction, which *eta* profile is overlapped. Example of improvements in the continuation of reflections is encircled in red for both sections when applying different NMO corrections.

wave data recording both spatially but also temporally. Earlier vertical component data for the retrieval of shear wave reflections partly suffered spatial aliasing because of their coarse receiver and shot spacing of 2–4 m (Malehmir *et al.* 2013a). The current setup, although with a no fold coverage in the middle of profile, partly overcomes this problem and resulted in the best image of the reflection *S*2 observed so far along the line (Fig. 7). The *S*-*S* wavefield seismic sections show ultrahigh resolution, based on the dominant frequency measured for the *S*1 and *S*2 reflections (40–60 Hz), and given a velocity of 60–80 m s^{-1}, this leads to 0.5–1 m resolution based on the quarter of wavelength criteria. This is also consistent with the borehole information (Salas-Romero *et al.* 2016) showing a separation between *S*1 and *S*2 of approximately 7 m, and resolved only by the *S*-*S* sections. The *S*2 reflection is generated from a coarse-grained layer, similar to *S*1, characterized by Salas-Romero *et al.* (2016, 2019) based on borehole logging and direct soil sampling. The coarse-grained materials, mainly sand and silt, show low natural gamma and high magnetic susceptibility due to the presence of some magnetic grains within them. Interestingly, along Line 1, most quick clays occur overlying these coarse-grained materials showing why high-resolution reflection imaging, as presented in this study, is important. From geotechnical point of view, the *Vp*/*Vs* ratio is the best indicator for water content and can simply be calculated using reflection traveltimes, *ts*/*tp*, picked from the seismic sections for identical horizons. While an average value, this ratio is valuable and simple to estimate. The *Vp*/*Vs* profile overlapped on the migrated sections in Figs 7(c) and (d) suggests high *Vp*/*Vs* values on the order of 11–16, which is quite high for any construction purposes.

Depending on the receiver–source orientations, a non-uniform delineation of different layers indicates a complex wave propagation in the medium. Shallower sediments (likely also silty-sandy) overlying *S*1 are imaged and manifest themselves more of flat-depositional features in H_R-V, V-H_T and H_T-H_T, while *S*1 and *S*2 appear to have suffered consolidation and show concave shapes. It is possible that *S*1 and *S*2 are larger in thickness, hence, have suffered more from normal consolidation than the sediments above.

5.1 Origin of the shear wave reflections

Given the completeness of the data, H_R-H_R and H_T-H_T images can likely contain most of the pure-shear wave reflections (Fig. 6b, middle section, and c, bottom section). However, given the large near-surface elastic property contrasts, significant shear wave energy is also generated in even the vertical component data. Wave radiation patterns for *P*- and *S*-wave sources generated on the surface using the properties of the medium support this claim (Fig. 8). Tang *et al.* (1994), Gaiser (2019) and Pugin & Yilmaz (2019) have also reported similar observations from different regions in the world. The

Downloaded from https://academic.oup.com/gji/article/235/3/2094/7269211 by Uppsala Universitetsbibliotek user on 22 November 2023

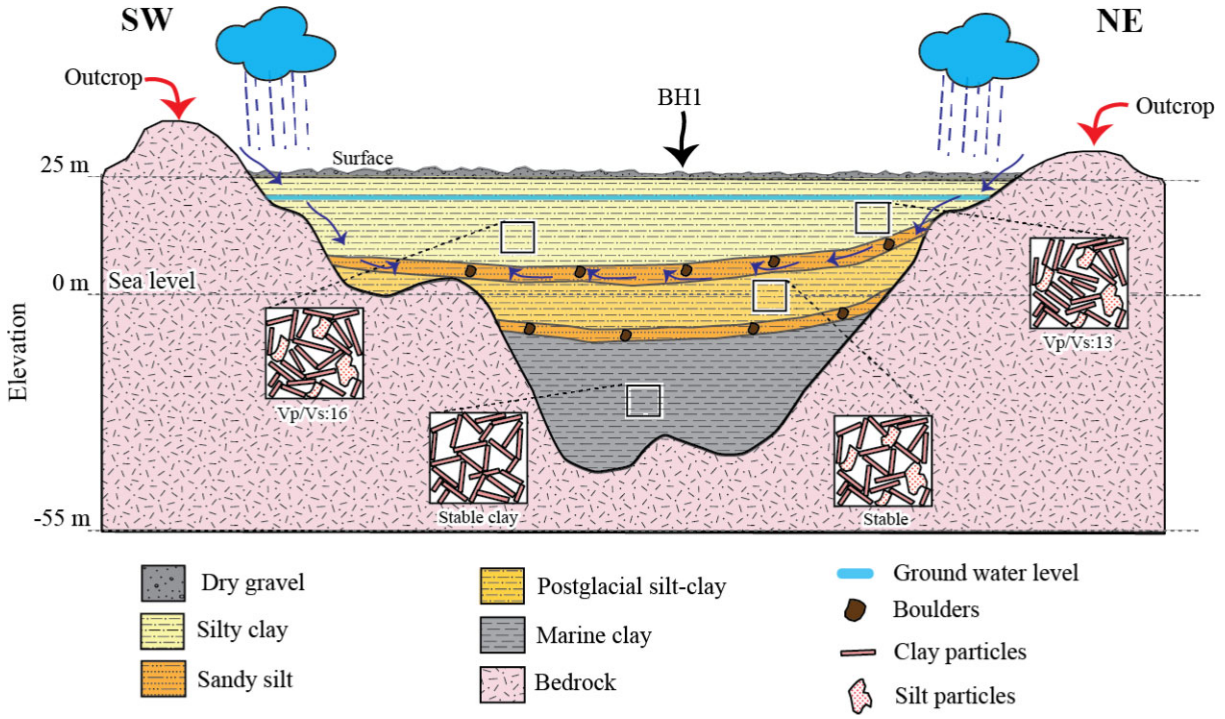

Figure 11. Sketch of the geological section, water flow model and clay structure along the line. Bedrock shows an undulated-shape with overlying clay to silt, which are slightly tilted towards the southwest. Sandy-silty layers with interbedded clayey materials, which may play a role in the leaching process and circulation of fresh water towards the clays. Given the water flow path and *Vp*/*Vs* ratio, the clay-grained structure is suggested to be of a 'house of cards' when in stable status, while aligned-grain structure when clay sensitivity increases. This also implies less water content, lower *Vp*/*Vs*, and higher degree of anisotropy for quick or sensitive clays composed to undisturbed clays.

models used for plotting the radiation patterns employ a *P*-wave velocity of 1400 m s^{-1} and varying *S*-wave velocities of 100, 150 and 200 m s^{-1}. As evidently shown in Fig. 8, due to the extremely slow shear wave velocity of the site, much of the energy radiates in the medium is of shear nature even for a vertically displacing seismic source. Hardage & Wagner (2018), Gaiser (2019) and Pugin & Yilmaz (2019) suggested that the higher the *Vp*/*Vs* ratio the easier for *P*-wave energy to be consumed. Vertical sources generate *S*-wave energy with lobs showing a take-off angle of $\pm$ 30° (Fig. 8a) implying a narrow offset presentation of them (Fig. 3). Horizontal sources produce broader *S*-wave energy (Fig. 8b), hence can better sample the subsurface for shear wave reflections. While vertical sources should not generate shear wave energy in the transverse direction, because of the high *Vp*/*Vs* ratio (like of a muddy/gel material), it is even possible that shear displacements occur in both horizontal planes making it hard to judge if the shear reflections are of *SV* or *SH* nature. Careful inspection of the shot gathers shown in Fig. 3, however, suggests that the vertical source generated better reflections in the transverse component while other wave modes (e.g. *P*-*S* and *S*-*P*) are better seen in the radial component. One reason why the horizontal sources have failed to provide super quality shear wave reflection sections can be due to the difficult ground coupling of the H-shaped base plate. Nonetheless, H_T-H_T configuration still provides a good quality image (Figs 7b and d), since it is less complicated in terms of wavefield propagations and wave mode leakage from one mode to another.

5.2 Anisotropy contributions

Differences in reflection traveltimes for various source–receiver orientations suggest a complex wavefield propagation and sensitivity to the subsurface materials (Crampin *et al.* 1984; Crampin 1985). Due to better consistency along reflection B, we focus on its traveltimes in different source–receiver orientations as shown in Fig. 9. A slow shear wave is captured for the bedrock reflection in the V- and H_R-receiver components when a H_T-source is excited; likewise for the V-V source–receiver orientation. The fastest shear wave reflection is recorded in the V-receiver component when the source is H_R (radial). This implies that *SV*-*SV* wave mode is recorded in the vertical component data and have the fastest bedrock shear wave arrivals at about 60 ms earlier than most other source–receiver configurations. This traveltime delay is more significant on the northeast of the line where bedrock comes closer to the surface. Despite the small shear wave wavelength in the medium, it is not surprising that this seemingly layered clay setting has a contribution of seismic anisotropy, thus a further question rises if this could have influenced the imaging workflow and could be further scrutinized in the data.

Fig. 10(a) shows an example NMO-corrected CDP gather as a function of offset. It is evident that far offsets are not well corrected as usually observed in large-scale studies of sedimentary basins and in anisotropic settings. Fig. 10 shows unmigrated stacked section of the vertical-source–receiver orientation processed using conventional NMO-based (Fig. 10a) compared to NMO4-based corrections (Fig. 10b). As a result, some *S*-*S* reflections show improved continuity. In order to understand lateral variations of the section, *eta* parameter (ζ) is plotted on the section of Fig. 10(d). Interestingly, *eta* parameter shows the highest value where bedrock reflection shows the largest traveltime delays. Given *S*-wave slowness isotropic when $\zeta = 0$, along the V-V source-receiver orientation section, ζ ranges between 0.1 and 0.4 indicating the level of anisotropy being weak-to-moderate $\zeta \leq 0.2$ (Thomsen 1986; Alkhalifah & Tsvankin 1995).

Downloaded from https://academic.oup.com/gji/article/235/3/2094/7269211 by Uppsala Universitetsbibliotek user on 22 November 2023

Based on recent update of the geohazard map from the Swedish Geotechnical Institute, the area where our studies are performed is of high risk of quick-clay landslide. Fig. 11 shows a geological sketch along Line 1, which is based on these results, borehole drilling data and soil sample studies from BH1. We attribute the higher degree of *S*-wave anisotropy near the bedrock on the northeast of the line as indication for partly collapsed clay structure or presence of quick clays. The 9C data set while has much more potential for other wave modes, already shows great potential for quick-clay landslide studies and we highly recommend them. Future studies will exploit if *P*-*S* and *S*-*P* wave modes can also be implemented and used for the interpretation of the data.

6 CONCLUSIONS

We have acquired a 9C seismic data set over a quick-clay landslide prone area showing ultrahigh-resolution quality data. The data set allows imaging the stratigraphical column all the way to bedrock with a resolution on the *S*-*S* section on the order of 0.5–1 m. A fine receiver spacing for shot points and receiver positions of 1 m helped to acquire less aliased *S*-*S* wavefield data compared to the previous works at the site. Two distinct sets of reflections, *S*1 and *S*2, interpreted to be from coarse-grained materials and a third one, B, from bedrock were imaged in the *S*-*S* sections. *S*-*S* wavefield sections were captured in different quality in different source–receiver orientations helping to identify V-H_T and H_T-H_T as the optimal source–receiver orientations for *S*-*S* wavefield imaging. Given the higher sensitivity of shear waves to anisotropy, this effect was investigated by applying a non-hyperbolic NMO. The incorporation of the anisotropy term in the NMO corrections in the seismic processing workflow led to improvements in the continuity of some of the reflections. The areas with this anisotropic sensitivity is observed to coincide with places where *Vp*/*Vs* ration is rather lower implying a partial collapsed clay structures or presence of quick clays. The 9C data set is rich in information and has greatly improved our understanding of the subsurface structures and its elastic properties and the environment in which quick clays are present.

ACKNOWLEDGMENTS

The seismic data acquisition that allowed this study was sponsored by the Society of Exploration Geophysicist (SEG) Foundation. We thank PhD students and post-docs from Uppsala University who contributed into the data acquisition and preparation of the data. We thank two anonymous reviewers along with the associate editor for their critical comments that helped to improved quality of our work.

DATA AVAILABILITY

Research data will be available after exploiting the potential of the seismic source and the data set by the team initiated the project and idea. There is currently an embargo time of 3-yr on the data. Contact alireza.malehmir@geo.uu.se for further instructions.

REFERENCES

Adamczyk, A., Malinowski, M. & Malehmir, A. 2014. High-resolution near-surface velocity model building using full-waveform inversion–a case study from southwest Sweden, *Geophysical Journal International,* **197,** 1693–1704.

Alkhalifah, T., 1997. Seismic data processing in vertically inhomogeneous TI media, *Geophysics,* **62,** 403–692.

Alkhalifah, T. & Tsvankin, I., 1995. Velocity analysis for transversely isotropic media, *Geophysics,* **60,** 1550–1566.

Ata, E. & Michelena, R.J., 1995. Mapping distribution of fractures in a reservoir with *P*-*S* converted waves, *Leading Edge,* **14,** 664–676.

Bansal, R. & Gaiser, J., 2013. An introduction to this special section: applications and challenges in shear-wave exploration, *Leading Edge,* **32,** 1–120.

Brigatti, M.F., Galan, E. & Theng, B.K.G., 2006. Structures and Mineralogy of clay minerals, in *Handbook of Clay Science,* pp. 19–86, eds Bergaya, F. & Theng, B., Elsevier.

Brodic, B., Malehmir, A., Juhlin, C., Dynesius, L., Bastani, M. & Palm, H., 2015. Multicomponent broadband digital-based seismic landstreamer for near-surface applications, *J. appl. Geophys.,* **123,** 227–241.

Crampin, S., 1985. Evaluation of anisotropy by shear-wave splitting, *Geophysics,* **50,** 142–152.

Crampin, S., Chesnokov, E. & Hipkin, R., 1984. Seismic anisotropy – the state of the art: II, *Geophys. J. Int.,* **76,** 1–16.

Dasios, A., McCann, C., Astin, T.R., McCann, D.M. & Fenning, P., 1999. Seismic imaging on the shallow subsurface: shear-wave case histories, *Geophys. Prospect.,* **47,** 565–591.

Farfour, M. & Yoon, W., 2016. A review on multicomponent seismology: a potential seismic application for reservoir characterization, *J. Adv. Res.,* **7,** 515–524.

Gaiser, J., 2019. Modelling S wave radiation for SP waves in isotropic and anisotropic media, *Geophys. Prospect.,* **67,** 2414–2431.

Gupta, M., DeAngelo, M.V. & Hardage, B., 2015. P-P and S-S wave interpretation of a carbonate formation: a case study from the Arbuckle interval in Wellington field, Kansas, in *SEG Technical Program Expanded Abstracts,* pp. 2082–2087.

Gylland, A., Long, M., Emdal, A. & Sandven, R. 2013. Characterisation and engineering properties of Tiller clay, *Engineering Geology,* **164,** 86–100.

Hardage, B., DeAngelo, M.V., Murray, P.E. & Sava, D., 2011. *Multicomponent Seismic Technology,* Society of Exploration Geophysicists, 335pp.

Hardage, B. & Wagner, D., 2018. Direct-SV radiation produced by land-based P-sources—Part 1: surface sources, *Interpretation,* **6,** T569–T584.

HU, T.-Y., Zhang, G.-J., Zhao, W. & Wen, S.-L., 2004. Decomposition of multicomponent seismic wavefields, *Chin. J. Geophys.,* **47,** 572–576.

Kristiansen, P. & Waggoner, J., 2005. Using multicomponent seismic data to better characterize and manage reservoirs, *Petrol. Geol. Conf. Ser.,* **6,** 1377–1384.

Li, X.-Y. & Yuan, J., 2003. Converted-wave moveout and conversion-point equations in layered VTI media: theory and application, *J. appl. Geophys.,* **54,** 297–318.

Li, X.-Y. & Zhang, Y.-G., 2011. Seismic reservoir characterization: how can multicomponent data help?, *J. geophys. Eng.,* **8,** 123–141.

Lundberg, E., Malehmir, A., Juhlin, C., Bastani, M. & Andersson, M. 2014. High-resolution 3D reflection seismic investigation over a quick-clay landslide scar in southwest Sweden, *Geophysics,* **79,** B97–B107.

Lundström, K., Larsson, R. & Dahlin, T. 2009. Mapping of quick clay formations using geotechnical and geophysical methods, *Landslides,* **6,** 1–15.

Malehmir, A., 2019. Recording longer for higher-resolution near-surface imaging-shear-wave reflections from vertical sources and receivers, in *Near Surface Geoscience Conference & Exhibition Conference Paper,* pp. 1–5.

Malehmir, A., 2021. The forgotten shear/wave reflections in the compressional/wave surveys, in *European Association of Geoscientists & Engineers Conference Paper,* pp. 1–5.

Malehmir, A., Bastani, M., Krawczyk, M., Gurk, M., Ismail, N., Polom, U. & Persson, L., 2013a. Geophysical assessment and geotechnical investigation of quick-clay landslides-a Swedish case study, *Near Surf. Geophys.,* **11,** 341–350.

Malehmir, A., Saleem, M.U. & Bastani, M., 2013b. High-resolution reflection seismic investigations of quick-clay and associated formations at a landslide scar in southwest Sweden, *J. appl. Geophys.,* **92,** 84–102.

Downloaded from https://academic.oup.com/gji/article/235/3/2094/7269211 by Uppsala Universitetsbibliotek user on 22 November 2023

Malehmir, A., Socco, L. V. Bastani, M. Krawczyk, C. M. Pfaffhuber, A. A. Miller, R. D. Maurer, H. & Frauedfelder, R. 2016b. *Chapter Two - Near-surface geophysical characterization of areas prone to natural hazards: a review of the current and perspective on the future: Advances in Geophysics,* Elsevier, Amsterdam, Netherlands. doi: 10.1016/bs.agph.2016.08.001.

Miles, D.R., 1988. Three-component seismic data: researcher's toy or interpreter's tool?, *Leading Edge,* **7,** 1–64.

Miller, G.F. & Pursey, H., 1954. The field and radiation impedance of mechanical radiators on the free surface of a semi-infinite isotropic solid, *Proc. R. Soc. Lond.,* **223,** 521–554.

Odenstad, S., 1958. Jordskredet I Göta den 7 juni 1957, *Geol. Fören. Stockh. Förh.,* **80,** 76–86.

Pertuz, T. & Malehmir, A., 2021. Ultra-high-resolution multicomponent seismic imaging of a quick-clay landslide-prone area in southwest of Sweden, in *SEG Technical Program Expanded Abstracts,* pp. 1811–1815.

Pertuz, T. & Malehmir, A., 2023. Ultra-high-resolution shear-wave reflection imaging of vertical component data in a quick-clay prone to landslide area in southwestern Sweden, *Geophysics,* **88,** 1–61.

Polom, U., Bagge, M., Wadas, S., Winsemann, J., Brandes, C., Binot, F. & Krawczyk, C.M. 2013. Surveying near-surface depocentres by means of shear wave seismics, *First Break,* **31,** 67–79.

Pugin, A., Larson, T., Bergler, S., McBride, J. & Bexfield, C., 2004. Near-surface mapping using SH-wave and P-wave seismic land-streamer data acquisition in Illinois, U.S., *Leading Edge,* **23,** 677–682.

Pugin, A., Pullan, S. & Hunter, J., 2009. Multicomponent high-resolution seismic reflection profiling, *Leading Edge,* **28,** 1248–1261.

Pugin, A. & Yilmaz, Ö., 2019. Optimum source-receiver orientations to capture PP, PS, SP, and SS reflected wave modes, *Leading Edge,* **38,** 45–52.

Qian, Z., Chapman, M., Li, X.-Y., Liu, E., Zhan, Y. & Wang, Y., 2007. Use of multicomponent seismic data for oil-water discrimination in fractured reservoirs, *Leading Edge,* **26**. doi:10.1190/1.2780789.

Salas-Romero, S., Malehmir, A., Snowball, I. & Brodic, M., 2021. Geotechnical site characterization using multichannel analysis of surface **waves**: a case study of an area prone to quick-clay landslides in southwest Sweden, *Near Surf. Geophys.,* **19,** 699–715.

Salas-Romero, S., Malehmir, A., Snowball, I. & Dessirier, B., 2019. Subsurface structures revealed using land-river reflection seismic data, *Solid Earth,* **10,** 1685–1705.

Salas-Romero, S., Malehmir, A., Snowball, I., Lougheed, B.C. & Hellqvist, M., 2016. Identifying landslide preconditions in Swedish quick clays – insights from integration of surface geophysical, core sample- and downhole property measurements, *Landslides,* **13,** 905–923.

Sayers, C. & Den Boer, L., 2016. The elastic anisotropy of clay minerals, *Geophysics,* **81,** 1–11.

Shan, C., Bastani, M., Malehmir, A., Persson, L. & Engdahl, M. 2014. Integrated 2D modeling and interpretation of geophysical and geotechnical data to delineate quick clays at a landslide site in southwest Sweden, *Geophysics,* **79,** 61–75.

Solberg, I.-L., Long, M., Baranwal, V.C., Gylland, A.S. & Rønning, J.S., 2016. Geophysical and geotechnical studies of geology and sediment properties at a quick-clay landslide site at Esp, Trondheim, Norway, *J. Eng. Geol.,* **208,** 214–230.

Stewart, R., 1994. The present and promise of P-S seismic exploration, *CREWES Res. Rep.,* **6,** 1–31.

Stewart, R., Gaiser, J., Brown, R. & Lawton, D., 2003. Converted-wave seismic exploration: applications, *Geophysics,* **68,** 40–57.

Tang, X., Zhu, Z. & Toksoz, M., 1994. Radiation patterns of compressional and shear transducers at the surface of an elastic half-space, *J. acoust. Soc. Am.,* **95,** 71–76.

Thomsen, L., 1986. Weak elastic anisotropy, *Geophysics,* **51,** 1954–1966.

Torrance, J., 2012. *Landslides: Types, Mechanisms and Modeling,* Cambridge Univ. Press, 436pp.

Tsvankin, I., 2005. *Seismic signatures and analysis of reflection data in anisotropic media*. second edition., Elsevier science.

Wang, S., Malehmir, A. & Bastani, M. 2016. Geophysical characterization of areas prone to quick-clay landslides using radio-magnetotelluric and seismic methods, *Tectonophysics,* 677–678. doi:10.1016/j.tecto.2016.04.020.

Weaver, C.E. & Pollard, L.D., 1973. *The Chemistry of Clay Minerals,* Elsevier, 212pp.

Yilmaz, O., Gao, K., Delic, M., Xia, J., Huang, L., Jodeiri, H. & Pugin, A., 2022. A reality check on full-wave inversion applied to land seismic data for near-surface modeling, *Leading Edge,* **41,** 2–72.

Downloaded from https://academic.oup.com/gji/article/235/3/2094/7269211 by Uppsala Universitetsbibliotek user on 22 November 2023

© The Author(s) 2023. Published by Oxford University Press on behalf of The Royal Astronomical Society. This is an Open Access article distributed under the terms of the Creative Commons Attribution License (https://creativecommons.org/licenses/by/4.0/), which permits unrestricted reuse, distribution, and reproduction in any medium, provided the original work is properly cited.